A Novel Approach for Room-Temperature Intersubband Transition in GaN HEMT for Terahertz Applications

Rakesh Kaneriya, Gunjan Rastogi, Palash Basu,
Rajesh Upadhyay and Apurba Bhattacharya

Abstract

Terahertz (THz) technology has attracted tremendous attention recently due to its promising applications in various domains such as medical, biological, industrial imaging, broadband, safety, communication, radar, space science, and so on. Due to non-availability of powerful sources and highly sensitive and efficient detectors, the so-called THz gap remains largely unfilled. Despite seamless efforts from electronics and photonics technology researchers, the desired level of technology development to fill the THz gap still remains a challenge. GaN-based HEMT structures have been investigated as potential THz sources and detectors by a number of researchers. This chapter presents a very new and versatile mechanism for electrical tuning of intersubband transitions (ISBT) GaN high electron mobility transition (HEMT) devices. ISBT phenomena are usually demonstrated in photonic devices like a quantum cascade laser (QCL). Here we explore ISBT in an electronic GaN HEMT device. Conventional photonic devices like a QCL are operated at cryogenic temperature to minimize thermal effect. Tuning the conduction band through external gate bias is an advantage of an HEMT device for room temperature (RT) THz applications. This chapter demonstrates the theoretical and experimental novel ISBT phenomenon in GaN HEMT is for potential ambient applications in the THz range.

Keywords: GaN HEMT, terahertz device, Intersubband transition, Plasmonic Metamaterials, quantum well

1. Introduction

Terahertz (THz) radiation is a small portion of the electromagnetic spectrum lying between the microwave and infrared regions. There is no precise range defining THz band, but it is most often –considered as frequencies in the range of 0.3–3.0 THz. Although sometimes it refers to 0.1–10 THz as well. The THz spectral range has drawn tremendous attention recently due to its promising applications in various domains. For example, in the field of biomedicine, THz radiation has been explored to detect various biomaterials like nucleic acids, proteins, cells and tissue applications [1, 2]. In the field of medical applications, the THz system has been demonstrated as a highly effective technique in cancer imaging, particularly for skin

cancer [3, 4]. A portable real-time THz imaging system could be used to assist early detection of diseases during routine health checkups. Since many non-metallic, non-polar materials are transparent to THz radiation, scanning of humans is feasible with no health hazards. Due to this, THz radiation is widely used for security and public safety applications. THz radiation can detect concealed weapons, explosives (e.g., C-4, HMX, RDX and TNT), illicit drugs (e.g., methamphetamine and heroin), and more [1]. THz imaging has become a valuable characterization tool for non-destructive testing, process control and quality inspection for inspection of silicon solar cells, nanocomposites, polymer films and dielectric films [1, 5, 6]. Space- and ground-based THz instruments have been explored significantly in the field of astronomy. For example, the THz system is extensively used to study the origin of the universe, formation of stars and galaxies, composition of planets and planetary atmospheres, the climate and environmental balance of our planet Earth, and more [7, 8].

Despite these tremendous potential applications, the so-called THz Gap is not fulfilled to the required level due to technology requirements of high-power sources and efficient and sensitive detectors in the THz range. Semiconductor devices and circuits like transistor and frequency multipliers work well towards the low end of THz frequency, but their power level drops off precipitously as the frequency increases. These devices can be operated up to ~1 THz with very low power. Conversely, semiconductor photonic devices like lasers can be utilized in the high-frequency THz range. Again, lasers are limited due to the non-availability of lower bandgap semiconductor materials towards low-frequency THz. The THz quantum cascade lasers (QCLs) showed promising results to fill this THz gap from 1 to 10 THz. However, QCLs required bulky cooling requirements, and reported maximum operating temperature is in the range of 150–200 K, which is too low for general applications [9, 10]. The demand for a compact, efficient and high-speed THz detector and source operating at room temperature has increased drastically. The non-availability of a room-temperature THz source and detector is a prime limitation of the modern THz system.

In this chapter, novel theoretical models and experimental techniques for the intersubband transitions (ISBT) phenomenon are illustrated for ambient THz applications. Section 2 covers the theoretical models and simulations based upon plasmonic metamaterials-assisted ISBT and describes the GaN HEMT response towards the THz spectrum. Section 3 covers the fabrication and measurement of a GaN HEMT device. Section 4 is investigates ambient temperature ISBT in a GaN HEMT device.

2. Theoretical modeling and simulation strategy

In this section, we present our theoretical model based on ISBT, metamaterial and plasmonic phenomena for GaN HEMT THz applications [11–13]. We proposed a combined plasmonic and metamaterial-driven ISBT phenomenon as one of the possible modes that can extend GaN HEMT operating frequency well beyond its present cut-off frequency to the THz band. ISBT is the prime mechanism to explore as a potential mechanism for THz operation, while metamaterial and plasmonic effects improve the strength of ISBT in a GaN HEMT structure. Theoretical modeling started with the role of polarization in a wurtzite semiconductor followed by the self-consistent solution of Schrodinger and Poisson equations; k.p model and Fermi Golden rule are used to compute ISBT in the GaN HEMT structure. The size and geometry of an HEMT device act as THz metamaterial (this concept is explored in-depth in Section 2.4) and it couples THz radiation to two-dimensional electron gas (2DEG) inside a triangular quantum well. Further, very small gate lengths in the range of 100–250 nm are selected for high-frequency operation of HEMT. This fine

nanometric-sized gate structure of HEMT excites surface plasmon waves at the interface between the gate metallic contact and 2DEG channel in the GaN heterostructure (this concept is explored in-depth in Section 2.5). These combinations (i.e., plasmonic metamaterial-assisted ISBT) govern the THz response of the GaN HEMT device.

2.1 GaN heterostructure and device description

GaN heterostructure is generally grown on sapphire or silicon carbide (SiC) substrate. **Figure 1(a)** shows the most widely used GaN heterostructure, which consists of a 60-nm AlN nucleation layer, 2-μm thick undoped GaN layer, 1-nm AlN spacer layer, 20 nm-undoped $Al_{0.3}Ga_{0.7}N$ barrier layer, and 3-nm Si_3N_4 passivation layer. Introducing a thin 1-nm AlN interlayer between AlGaN and GaN plays a crucial role. Better carrier confinement, reduced alloy scattering and enhanced conductivity are achieved by inserting a thin AlN layer [14, 15]. The cross-sectional view of the simulated GaN HEMT device by Silvaco TCAD is shown in **Figure 1(b)**. Computation mesh to simulate the device structure is shown in **Figure 1(c)**. In the regions beneath the gate, at the edges of the source and drain contacts and at the AlGaN/AlN/GaN interface, fine meshing is done to achieve the convergence and accuracy of the calculations. The spacing between different electrodes, namely, source to gate, gate to drain and source to drain are set to 0.9, 2.0 and 3.0 μm, respectively. Gate length is kept as 100 nm. To obtain lower gate resistance, gate geometry is selected as T-gate in simulation as well as in fabrication.

Generally, high-power RF GaN HEMT is fabricated in a multi-finger configuration. Two ground-source-ground (GSG) configurations are shown in **Figure 2**: 2×150 and 8×150. To measure the RF performance of the device GSG configuration is widely used for HEMT fabrication. The 2×150 configuration contains two gate fingers with 150-micron unit gate width of the device. Similarly, the 8×150 configuration contains eight gate fingers with 150-micron unit gate width. To expand the device length for high-power applications, a greater number of gate fingers are used. For example, if the power handling capability of the fabricated GaN HEMT is 5 W/mm, the $2 \times 150 = 0.3$-mm device can be used for 1.5 W RF power. Similarly, the $8 \times 150 = 1.2$-mm device can be used for 6.0 W RF power. Before further discussion on plasmonic metamaterial-assisted ISBT, the following section refreshes some fundamentals about polarization in III-N (nitride) semiconductors.

2.2 Polarization in GaN heterostructure

The nitride semiconductor materials exhibit inherent polarization properties. Having the large ionicity of the nitride bond (Ga–N, Al–N, In–N, etc.), it possesses a
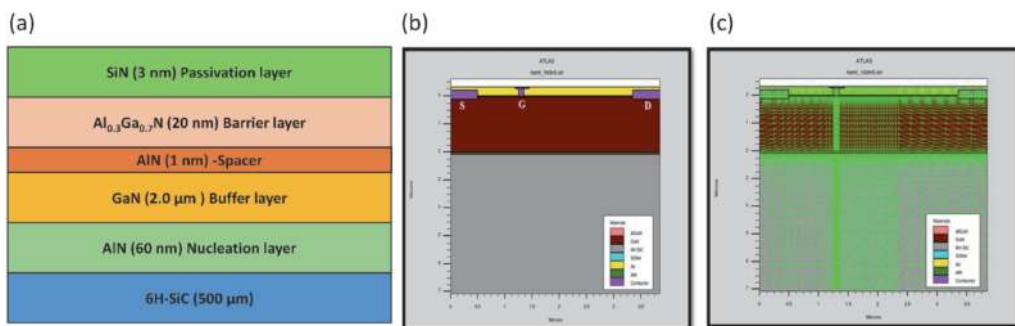

Figure 1.
(a) GaN Heterostructure, (b) HEMT cross-sectional view and (c) HEMT mesh structure (reprinted with permission from Ref. [12]).
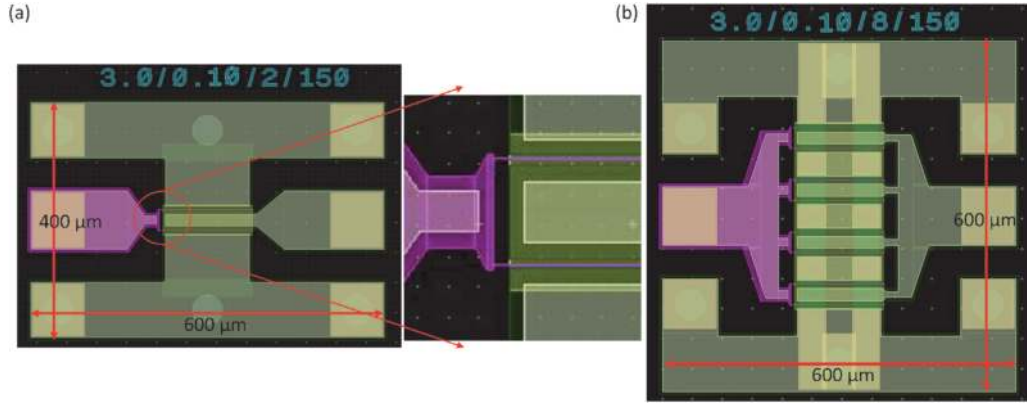
Figure 2.
Typical configurations of GaN HEMT (a) 2 gate fingers with 150 micron gate width (2 × 150) (zoom image for gate fingers visualization and (b) 8 gate fingers with 150 micron gate width (8 × 150). Representation 3.0/0.10/8/150 indicates source to drain distance 3.0 µm, 0.1 µm (100 nm) gate length, 8 fingers device with 150 µm gate width.

piezoelectric polarization (P_{PE}) component, while the absence of the center of inversion symmetry and uniaxial nature of the crystal structure produces spontaneous polarization (P_{SP}). Total polarization (P_T) in the nitride semiconductor heterostructure is a combination of spontaneous polarization (P_{SP}) and piezoelectric polarization (P_{PE}), as shown in Eq. (1).

$$P_T = P_{SP} + P_{PE} \tag{1}$$

Furthermore, the strain-induced effect at the interface between two nitride semiconductors enhances piezoelectric polarization in the heterostructure. Piezoelectric polarization of the crystal is generally defined in terms of strain (ε) and stress (σ) components. Stress and strain are correlated in a crystal by elastic coefficient $\varepsilon_{ij} = C_{ij}\,\sigma_{ij}$. The piezoelectric polarization in heterostructure grown along the z-axis (0001) is given by,

$$P_{PE} = E_{33}\varepsilon_z + E_{31}\left(\varepsilon_x + \varepsilon_y\right) \tag{2}$$

where E_{33}, and E_{31} are piezoelectric coefficients, and ε_x, ε_y and ε_z are strain in x, y and z-directions, respectively. The crystal edge length and height are represented as a_0 and c_0 respectively in a hexagonal crystal lattice. The strain along the x, y and z-axis is given by (in-plane strain along x-axis and y-axis are assumed to be isotropic),

$$\varepsilon_z = \frac{c - c_0}{c_0}, \varepsilon_x = \varepsilon_y = \frac{a - a_0}{a_0} \tag{3}$$

where a_0 and c_0 are the equilibrium or unstrained values of lattice constants and a and c are the strain lattice constant due to growth of heterostructure. For hexagonal lattice crystal, the strain components along ε_z and ε_x are related with elastic coefficients as per the following equation,

$$\varepsilon_z = -2\frac{c_{13}}{c_{33}}\varepsilon_x, \quad \frac{c - c_0}{c_0} = -2\frac{c_{13}}{c_{33}}\frac{a - a_0}{a_0} \tag{4}$$

where C_{13} and C_{33} are the elastic constants. Substituting Eqs. (3) and (4) in Eq. (2),

$$P_{PE} = 2\frac{a - a_0}{a_0}\left(E_{31} - E_{33}\frac{c_{13}}{c_{33}}\right) \tag{5}$$

The macroscopic piezoelectric polarization is defined by variations of the lattice constants a and c. The microscopic piezoelectric polarization is expressed in terms of an internal parameter u, defined as the anion–cation bond length along the z-axis (0001) [16]. Substituting elastic constant values for AlN and GaN in Eq. (5), one gets piezoelectric polarization of AlN greater than GaN. Spontaneous polarization closely depends upon crystal structure c/a ratio. The ideal c/a ratio in the hexagonal, closed-pack crystal structure is 1.633. The spontaneous polarization is found to be greater in actual crystal structures as the c/a ratio is different from its ideal value [16]. This nonideality of c/a ratio in AlN is also greater than GaN, which leads the greater spontaneous polarization. The spontaneous and piezoelectric polarization for alloy (i.e., AlGaN) is obtained by linear interpolation of the binary constituents (Vegard's law). In summary, the spontaneous and piezoelectric polarizations for AlGaN over the whole range of compositions are larger than that of a GaN buffer layer.

The polarization-induced charge density and sheet density in the heterostructure is given by,

$$\rho = -\nabla * P \tag{6}$$

$$\sigma = P_{T(Layer1)} - P_{T(Layer2)}$$

$$\sigma = \left[P_{SP(Layer1)} + P_{PE(Layer1)}\right] - \left[P_{SP(Layer2)} + P_{PE(Layer2)}\right] \tag{7}$$

The polarization-induced charge density and sheet density for the case of AlGaN/GaN heterostructure is given by,

$$\sigma = \left[P_{SP(GaN)} + P_{PE(GaN)}\right] - \left[P_{SP(AlGaN)} + P_{PE(AlGaN)}\right] \tag{8}$$

Extracted 2DEG concentration, purely due to polarization effects, is the order of $\sim 10^{13}$ cm^{-2} for nitride heterostructures. Unlike GaAs MODFET heterostructures, no doping is required in nitride heterostructures to generate 2DEG concentration, which is a great advantage of these structures.

The basic equations of physical processes are solved for every grid point in the simulation. These equations include Poisson's equation, continuity equations and transport equations, derived from Maxwell's equations [17]. The computation of 2DEG properties due to spontaneous and piezoelectric polarization effects is performed using a polarization model [18, 19]. An induced, strong polarization field is introduced to calculate band diagrams. To increase the reliability of simulation, measurement-based ohmic contact resistance and Schottky barrier height data were incorporated in the simulation to define source, drain and gate contacts. A low field mobility model is used to account for the temperature-dependent drift of electrons and holes separately [20]. The Shockley–Read–Hall recombination model is used to estimate the statistics of holes and electrons as well as their recombination rate. The traps/defects in the heterostructure play a crucial role in the performance of GaN devices. Accordingly, we also introduced interface traps energy level and density in the modeling. Output results were extracted by solving the basic equations for every grid point with the different biasing conditions. The variation of the drain current with respect to applied drain (Vd) and gate (Vg) biasing voltage is plotted in **Figure 3**. The simulated output characteristics (Id-Vd) and transfer characteristics (Id-Vg) are shown in **Figure 3(a)** and **(b)**, respectively. The extracted transconductance is >350 mS/mm as shown in **Figure 3(c)**. The extracted capacitance-gate

Figure 3.
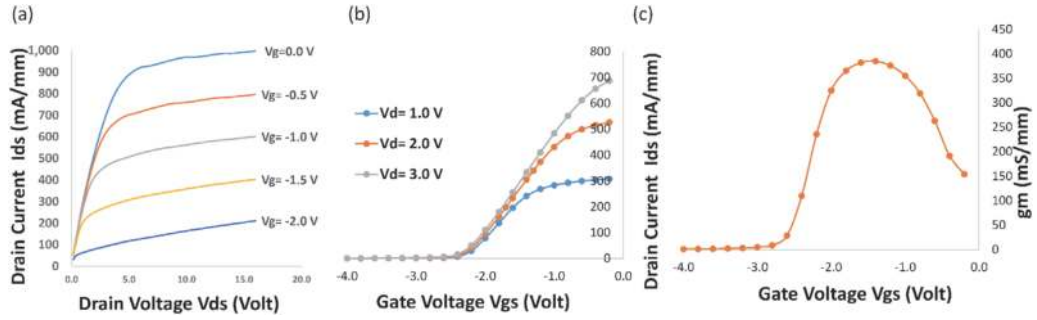*(a) Output characteristics (id-Vd), (b) transfer characteristics (id-Vg) and (c) Transconductance of the simulated device (reprinted with permission from Ref. [11]).*
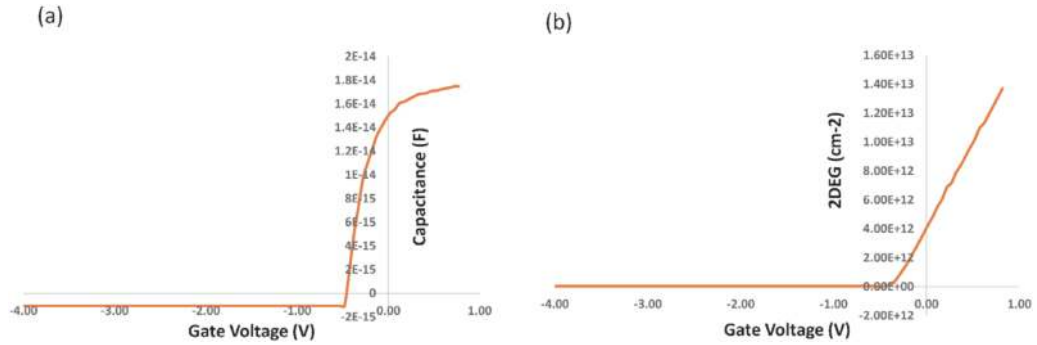

Figure 4.
Extracted (a) CV profile and (b) 2DEG profile with applied gate voltage (reprinted with permission from Ref. [12]).

voltage (Vg) and 2DEG density with applied gate bias are depicted in **Figure 4(a)** and **(b)**, respectively.

The current gain cutoff frequency (f_t) and maximum frequency of oscillations (f_{max}) are the two most pertinent parameters for high-speed device application. f_t and f_{max} are extracted from small signal RF simulation. Current gain (h_{21}) and maximum available power gain (G_a) are simulated at bias conditions Vds = 7 V and Vgs = −1.5 V and plotted with respect to frequency in **Figure 5**. A summary of simulated DC and RF device parameters is given in **Table 1** that closely matches the corresponding process design kit (PDK) datasheet of renowned international GaN foundries.

The cutoff frequency of field effect transistor (FET) including HEMT is defined by $f_T = v/2\pi L = 1/2\pi\tau$, where v is carrier velocity, L is gate length and τ is electron transit time under the gate. For very small gate length of 30 nm, up to 300–350 GHz cut-off frequency operation has been demonstrated [21]. However, beyond conventional transit-time limitations, these FET devices can be operated at much higher frequencies up to THz. Dyakonov–Shur proposed the plasma wave theory to describe THz behavior in FET devices [22, 23]. The basis of plasma wave theory is the instability of 2DEG, which has a resonant response to incident electromagnetic radiation in short-channel FET. The size and shape of the FET channel are used to govern the resonant response of plasma frequency to electromagnetic radiation. The tuning of plasmon frequency by external biasing has been used for detectors, mixers and multipliers [23]. There are several reports available in which the plasma wave theory is used to describe the THz behavior of devices. The plasma wave theory concept has been widely demonstrated in conventional semiconductors like Si [24], GaAs [22], GaN [25], and InP [26] as well as in new two-dimensional
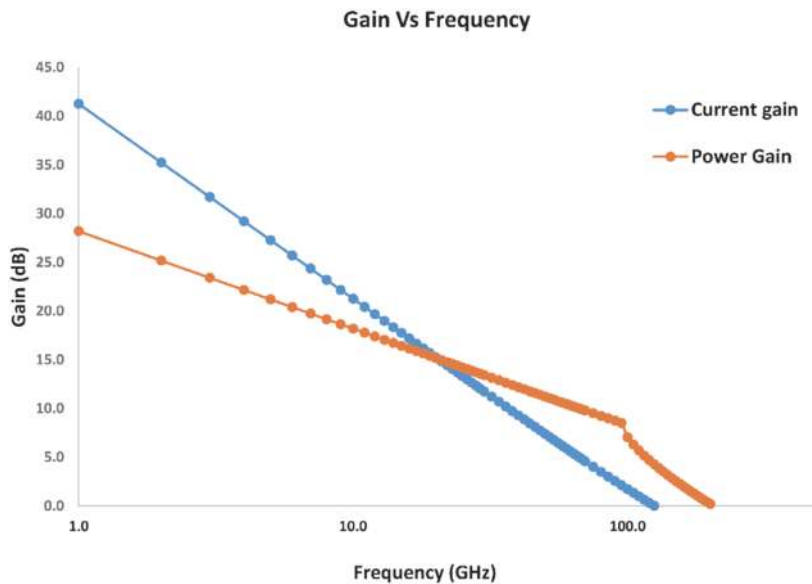
Gain Vs Frequency

Figure 5.
Current gain and power gain of the simulated device (reprinted with permission from Ref. [11]).

	Simulated result
Idss (A/mm)	0.995
Vknee (V)	5
Ron (ohm*mm)	3.5
Vth (V)	−3.0
gm (mS/mm)	384
ft (GHz)	110
fmax (GHz)	180

Table 1.
Summary of extracted DC and RF device parameters.

materials systems like graphene [27], black phosphorus [28], and more. There are a few papers available in which a working GaN HEMT mechanism is explained through plasma wave theory [25, 29–32]. Based on our simulation and experimental investigations, we have demonstrated for the first time that an ISBT mechanism, in addition to established plasma wave theory, can describe the THz behavior of a GaN HEMT device. ISBT theory is based on carrier transitions within a conduction band, which is entirely different from plasma wave theory. The fundamentals of this theory are explained below.

2.3 Quantum confinement in GaN heterostructure

The interaction between photons and electrons in the semiconductor can be expressed by the Hamiltonian,

$$H = \frac{1}{2m_0}(\mathrm{p} - \mathrm{eA})^2 + V(r) \qquad (9)$$

where m_0 is the free electron mass, $V(r)$ is the periodic crystal potential (in the present case it is the triangular potential function given by, $V(z) = eFz$), e is charge

of electron, Fz is electric field, and A is vector potential of applied electromagnetic field. Hamilton can be expanded into,

$$H = \frac{p^2}{2m_0} + V(r) - \frac{e}{2m_0}(\text{p.A} + \text{A.p}) + \frac{e^2 A^2}{2m_0} \tag{10}$$

$$H \approx H_0 + H'$$

Here H_0 is unperturbed Hamiltonian and H' is perturbed Hamiltonian due to the interaction of the electromagnetic wave.

Consideration of the strain effects for extraction of effective-mass Hamiltonian is of prime importance for wurtzite semiconductors. This Hamiltonian is used to derive the electronic band structures of bulk and quantum-well wurtzite semiconductors. Kane's model is applied to derive the band-edge energies and the optical momentum-matrix elements for strained wurtzite semiconductors. We then derive the effective-mass Hamiltonian by using the k.p perturbation theory. The developed k.p model is applied to our heterostructures structures, especially quantum well via the envelope function approximation (EFA) method [33, 34]. An envelope function model is derived for electrons in a semiconductor heterostructure. The materials-dependent Hamiltonian extraction by EFA method is most suitable for abrupt semiconductor junction [35]. The finite element method [36] is used to solve the coupled multi-band Schrödinger Poison's equation [37] numerically.

Under triangular quantum well, the solution of the wave function is given by [38, 39],

$$\Psi(z) = Ai \left[\frac{2m_z{}^* eF_z}{\hbar^2} \left(z - \frac{E_i}{eF_z} \right) \right] \tag{11}$$

where $m_z{}^*$ is the effective mass of electron in the GaN, Fz is the electric field in the z-direction, Ei is the eigenvalues of energy with i = 0,1,2, …. for the ground state, 1st excited state and so on. Airy (Ai) function is given by

$$Ai(z) = \frac{1}{\pi} \int_0^\infty \cos\left(\frac{t^3}{3} + zt \right) dt$$

The eigen value is given by [37, 38],

$$E_i \approx \left(\frac{\hbar^2}{2m_z{}^*} \right)^{1/3} \left[\frac{3\pi eF_z}{2} \left(i + \frac{3}{4} \right) \right]^{2/3} \tag{12}$$

When an incident THz radiation illuminates the GaN HEMT, electrons may absorb the photon energy and jump to a higher energy subband. Carriers below Fermi energy levels were collected by drain electrode when we applied voltage between source and drain. Using Fermi's golden rule for the transition from i state to j state, we can calculate the absorption coefficient by [34, 40],

$$W_{ij} = \frac{2\pi}{\hbar} < \Psi_i | H' | \Psi_j >^2 \delta\left(E_j - E_i - \hbar\omega \right)$$

where H' is interaction Hamiltonian as per Eq. (10).

By applying the dipole approximation, we obtain [34, 40],

$$W_{ij} = \frac{2\pi}{\hbar} \frac{e^2 E_0{}^2}{4m_z{}^2\omega^2} < i | e.p | j >^2 \delta\left(E_j - E_i - \hbar\omega \right) \tag{13}$$

The matrix element in the above equation can be expanded in terms of interband and ISBT as follows,

$$<i|e.p|f> \ = e. <u_v|p|u_{v'}> <f_n|f_{n'}> \ + e. <u_v|u_{v'}> <f_n|p|f_{n'}>$$

Applying the envelope function matrix element in the z-direction can be written as

$$<i|p_z|j> \ = \int \Psi_i^*(z) p_z \Psi_j(z) dz$$

The dimensionless optical field strength between the two-energy state is given by [33, 38],

$$f_{ij} = \frac{2}{m_z^* \hbar \omega_{ij}} <i|p_z|j>^2 = \frac{2m_0^* \omega_{ij}}{\hbar} <i|z|j>^2 \tag{14}$$

where $\omega_{ij} = (E_j - E_i)/2$
$<i/z/j>$ can be expressed as,

$$<i|z|j> \ = z_{ji} = \frac{2L}{(t_i - t_j)^2} \tag{15}$$

with, t_i and L are electric length expressed as,

$$t_i = \left[\frac{3\Pi}{2}\left(i + \frac{3}{4}\right)\right]^{2/3} \tag{16}$$

$$L = \left(\frac{\hbar^2}{2m_z^* eF_z}\right)^3 \tag{17}$$

By substituting Eqs. (15)–(17) in Eq. (14) we get,

$$f_{ij} = \frac{8.32}{(t_i - t_j)^4} \left(\frac{\Pi}{2}\right)^{2/3} \left[\left(j + \frac{3}{4}\right)^{2/3} - \left(i + \frac{3}{4}\right)^{2/3}\right] \tag{18}$$

By substituting i = 0 and j = 1,2,3, … oscillation strength for transition can be calculated as f_{01} = 0.73, f_{02} = 0.12, f_{03} = 0.045, and so on. The oscillator strength of all the transitions is sum up to 1. Calculated transition indicates that the probability for higher-level transitions is very weak.

The gradual pinning of Fermi level inside the quantum well is possible by increasing gate voltage. When gate voltage is sufficiently negative (0 > Vt > Vg), the conduction band is above the Fermi level. In this case, the channel is completely depleted of 2DEG. When the gate voltage is greater than the threshold voltage (Vg > Vt), charges start filling the channel. As the gate voltage increases, the Fermi level gradually pins inside the quantum well and 2DEG carriers are filled among allowed subbands in the channel. When gate voltage is sufficiently higher (Vg > 0 > Vt), the carrier occupies all allowed subband below the Fermi energy level. For this case, total 2DEG charges are distributed in the allowed energy subband and take participation in channel conduction. The triangular quantum-well conduction band energy profile for GaN HEMT with different gate biasing conditions is shown in **Figure 6(a)**. Fermi energy level pinning inside the subbands of triangular quantum well with different applied gate biasing is shown in
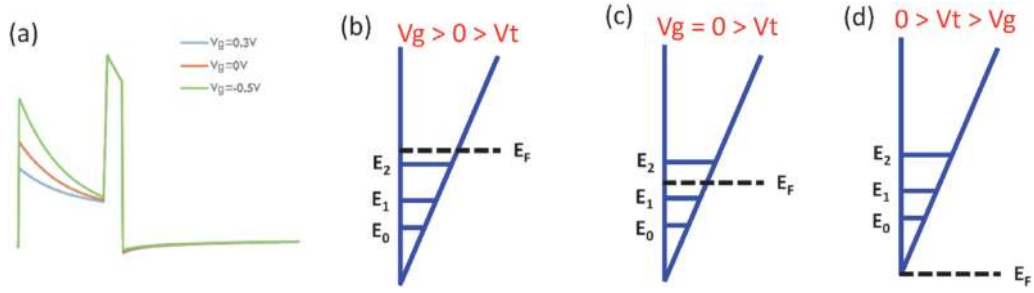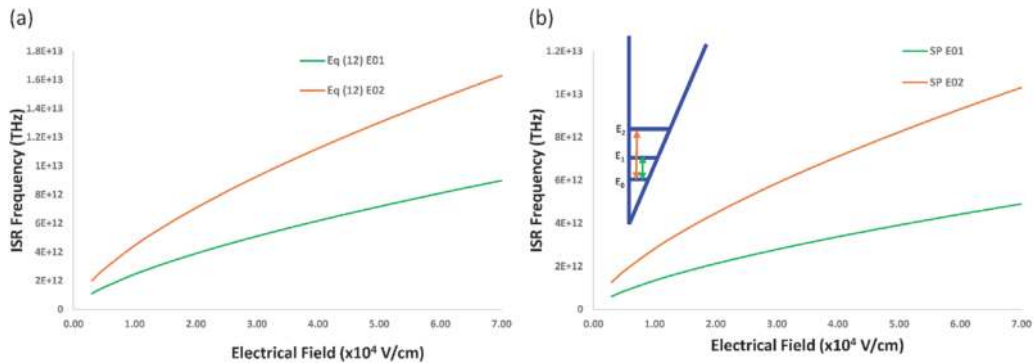
Figure 6.
Conduction band energy profile with different applied gate voltage and Fermi energy level with filled subband inside triangular quantum well with different applied gate biasing (b) Vg > 0 > Vt, (c) Vg = 0 > Vt and (d) 0 > Vt > Vg (reprinted with permission from Ref. [12]).

Figure 6(b)–(d). The spacing and charge filing inside the subband strongly depends upon gate-biasing voltage. In other words, the gate biasing-assisted tuning of intersubband resonance (ISR) frequency is possible in the HEMT structure.

In the simulation, we extracted up to four ISB energy levels inside the triangular quantum well. The ISR frequency as a function of applied gate-biasing field is calculated using Eq. (12) and by solving self-consistency Schrodinger–Poisson solver for different gate-biasing voltage. The same are shown in **Figure 7(a)** and **(b)**. The ISB tuning is one order higher in asymmetric triangular well potential as compared to the conventional square well potential. Moreover, 2DEG carrier concentration inside the GaN HEMT channel also depends upon Al composition and AlGaN barrier layer thickness. **Figure 8(a)** and **(b)** show the simulated 2DEG carrier concentration variation with AlGaN thickness and Al composition, respectively. It clearly indicates that increment in barrier layer thickness, and Al composition enhances the 2DEG density inside the channel. It further implies that manipulation in ISR is possible in GaN HEMT devices based on variation in 2DEG density, which provide tuning in the THz region.

2.4 Metamaterial-embedded ISBT

The combination of ISBT in semiconductor quantum wells with metamaterials shows great potential in the THz region [41–47]. There are large numbers of metamaterial structures that have been employed and demonstrated enhanced per-formance in the THz region. In the present modeling work, we report that the standard GSG device geometry of HEMT itself acts as a metamaterial structure. The enhancement of THz interaction with 2DEG inside the triangular quantum well is

Figure 7.
Intersubband resonance frequency as a function of the applied field (a) calculated using Eq. (12), (b) by solving self-consistency Schrodinger-Poisson solver. (reprinted with permission from Ref. [12]).
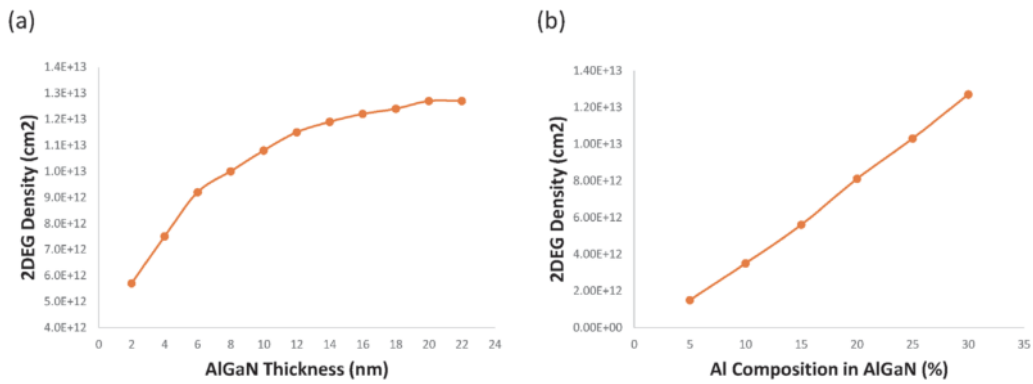
Figure 8.
2DEG carrier concentration of AlGaN/AlN/GaN heterostructure for (a) different AlGaN thickness, (b) different Al composition in AlGaN layer (reprinted with permission from Ref. [12]).

reported for GaN HEMT. The resonance mode in metamaterial structure is dynamically manipulating the carrier distribution inside the quantum well.

For the metamaterial modeling work, the GaN heterostructure and device geometry are kept identical, as shown in **Figure 1**. A finite difference frequency domain CST Microwave Studio simulator has been used to simulate the entire device configuration, which acts as THz metamaterial. Standard GSG configuration along with 50- to 150-micron gate width has been used for 3D electromagnetic modeling as shown in **Figure 9(a)–(c)**. Very fine localized tetrahedral sub-meshing has been used in the active source to drain region to enhance the accuracy of calculations as shown in **Figure 9(d)**. THz radiation (0.3–3 THz) is illuminated on the entire GSG device configuration, which includes the active GaN HEMT region as well. **Table 2** shows the dimensions used in 3D EM simulation work. Three different geometries, 2 × 50, 2 × 100 and 2 × 150, have been used in the present study. The E-field of the incident THz plane wave is kept at 1 V/m for all three devices.

The wavelength corresponding to the entire THz spectrum (0.3 to 10 THz) is about 30–1000 micron. If the device dimension is of the order of incident radiation, it acts as an antenna. Antenna size and shape largely determine the frequency it can handle. Antenna-coupled THz source and detector show a potential advantage in the performance of devices for the THz region [48–52]. The dimensions of the devices as listed in **Table 2** are of the order of illuminated THz radiation wavelength. These devices act as antennas, which leads to convergence of incident radiations towards the active channel region. The resultant electric field intensity inside the active channel region between source and drain is greatly enhanced. The enhancement of the field due to illumination strongly depends on the frequency of incident radiation and device dimension. For example, the electric field intensity distribution for 0.4 THz incident radiation is shown in **Figure 10** (a)–(c) for three different GaN HEMT devices. Each device structure has a unique resonance response towards incident THz radiation. Similarly, the resonance response of a 2 × 100 GaN HEMT device towards incident THz radiations, namely 0.3, 0.7 and 1.75 THz, is shown in **Figure 10(d)–(f)**. Moreover, the illumination-dependent enhancement of the field is not distributed uniformly throughout the channel. The highest field distribution found at the center of a 2 × 100 device for 1.75 THz illuminations is shown in **Figure 10(f)**. The summary for average field enhancement inside the channel region due to illumination is illustrated in **Figure 11**. The GaN HEMT device itself acts as metamaterial, which further influences the overall THz performance of the GaN HEMT device.
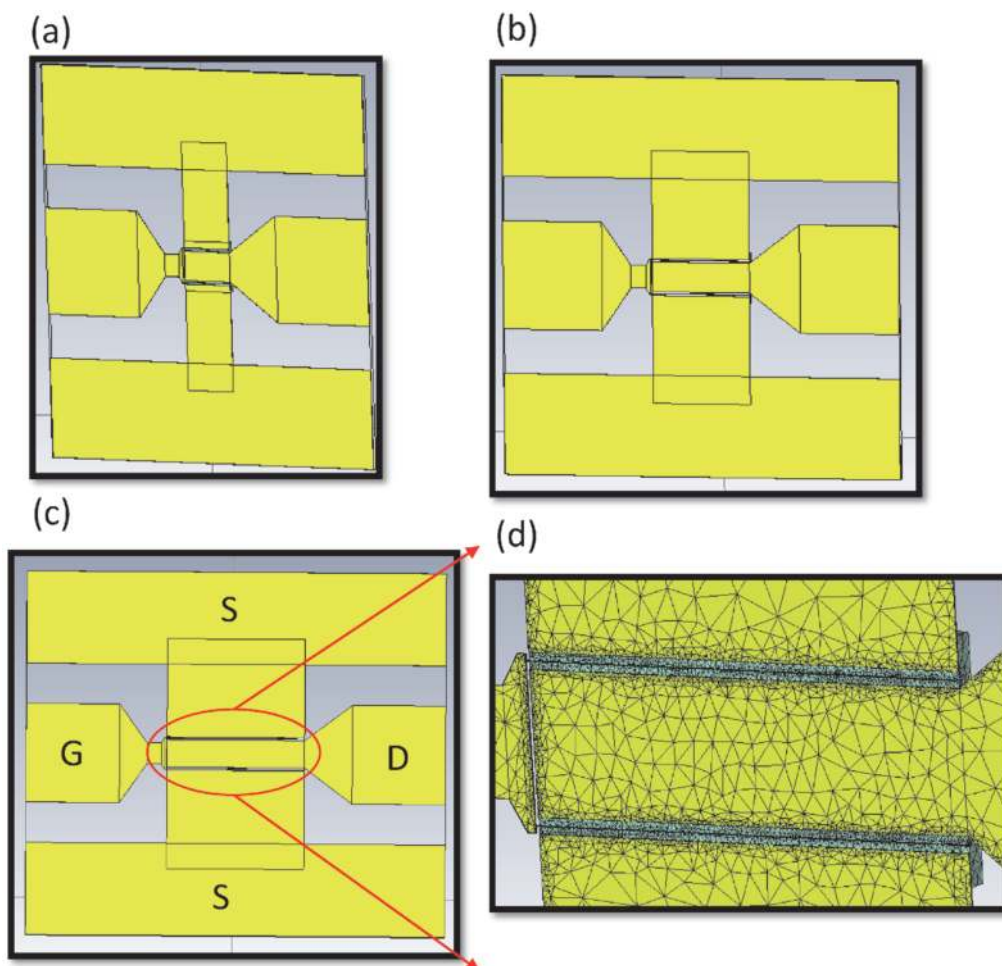
Figure 9.
Three different configuration (a) 2 × 50, (b) 2 × 100 and (c) 2 × 150 of GaN HEMT and (d) GaN HEMT meshing (reprinted with permission from URSI RCRS 2020, IEEE Xplore).

Device configuration	Distance between S and D (μm)	Gate width (μm)	Gate length (nm)	Total device dimension (μm x μm)
Device A (2 x 50)	3.0	50	100	350 x 400
Device B (2 x 100)	3.0	100	100	400 x 400
Device C (2 x 150)	3.0	150	100	450 x 400

Table 2.
Different device configurations used in simulations.

2.5 Plasmonic-assisted ISBT

A plasmonic nanostructure provides unique opportunities for manipulating electromagnetic waves in the THz range. Recently many novel plasmonic nanostructure-based devices such as photoconductor antennas [52, 53], detectors [31], and plasmonic photomixers [54], QCLs [55] showed significant improvement in device performance.

For plasmonic structure simulation, the finite element frequency domain COMSOL Multiphysics numerical method has been used to solve Maxwell's equation to predict electromagnetic interaction in each layer of the semiconductor
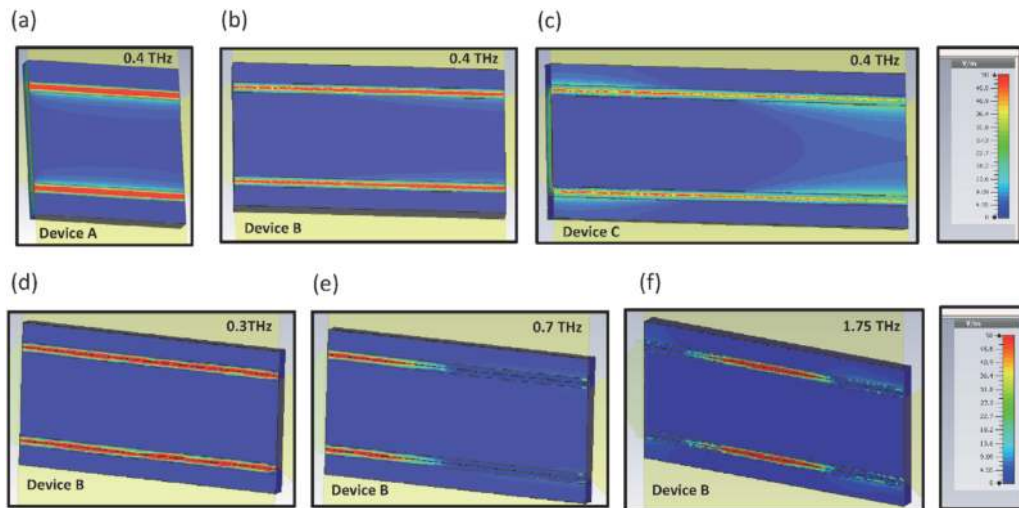
Figure 10.
Electrical field enhancement for 0.4 THz incident radiation on (a) 2 × 50, (b) 2 × 100 and (c) 2 × 150 of GaN HEMT devices. Electrical field enhancement for 2 × 100 GaN HEMT device at (d) 0.3°THz, (e) 0.7° THz and (f) 1.75°THz incident radiation (reprinted with permission from URSI RCRS 2020, IEEE Xplore).
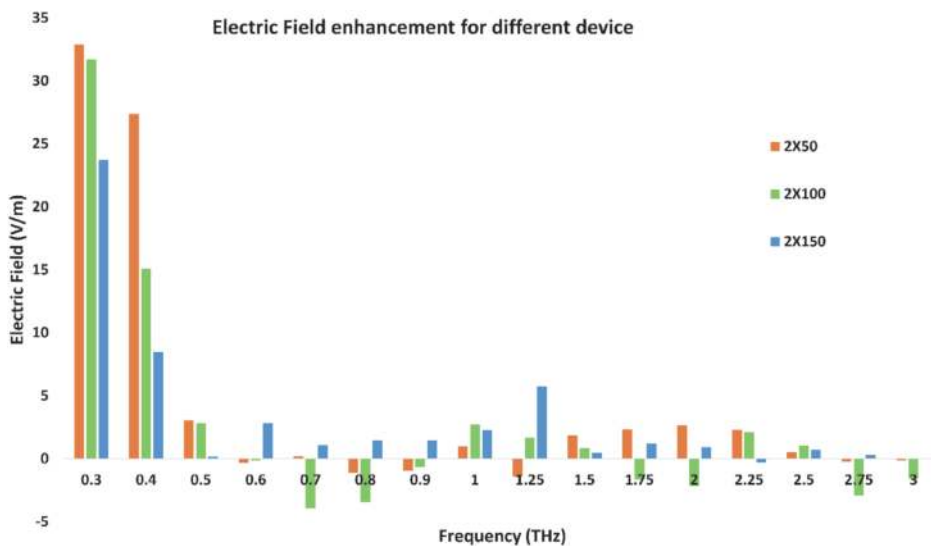

Figure 11.
Electrical field enhancement due to illumination of terahertz radiation on GaN HEMT devices.

heterostructure. Heterostructure stack, device geometry and device structure are kept identical as used in semiconductor modeling shown in **Figure 1**. We kept 1 V/m incident plane wave THz radiation from 0.3 to 3 THz to interact with the GaN heterostructure. The surface plasmon is generated at the interface between nanometric gate contact and heterostructure.

The field in the vicinity of the fine gate structure is drastically increased due to surface plasmon generation. Subsequently, the THz incident wave is coupled to 2DEG inside the channel. The concentration of the induced electric field is considerably enhanced in close proximity to the device gate contact electrodes. The induced electric field is approximately 5.5E+06 on the gate and 8.5E+06 V/m on the gate edge for 0.4 THz due to plasmonic structure as shown in **Figure 12**. As the incident frequency increases, the plasmonic-induced electric field also increases and saturates towards higher frequency as depicted in **Figure 13**. It was interesting to find that the plasmonic-enhanced field ($\sim 10^7$ V/m) is approximately one order
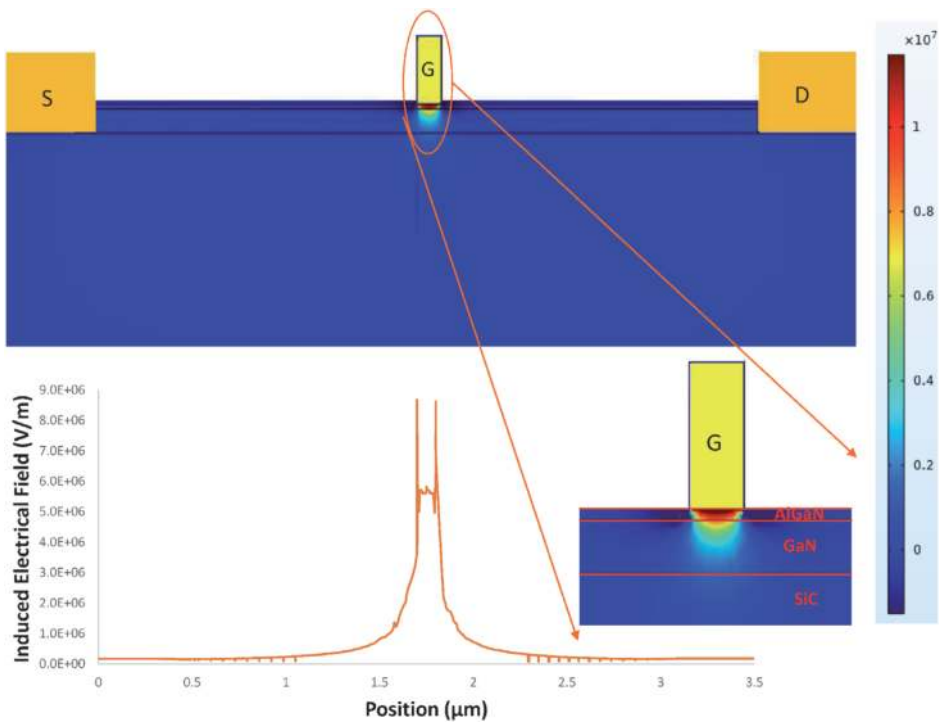
Figure 12.
Electrical field enhancement for 0.4°THz incident radiation on GaN HEMT device using a finite element method-based electromagnetic solver (COMSOL).
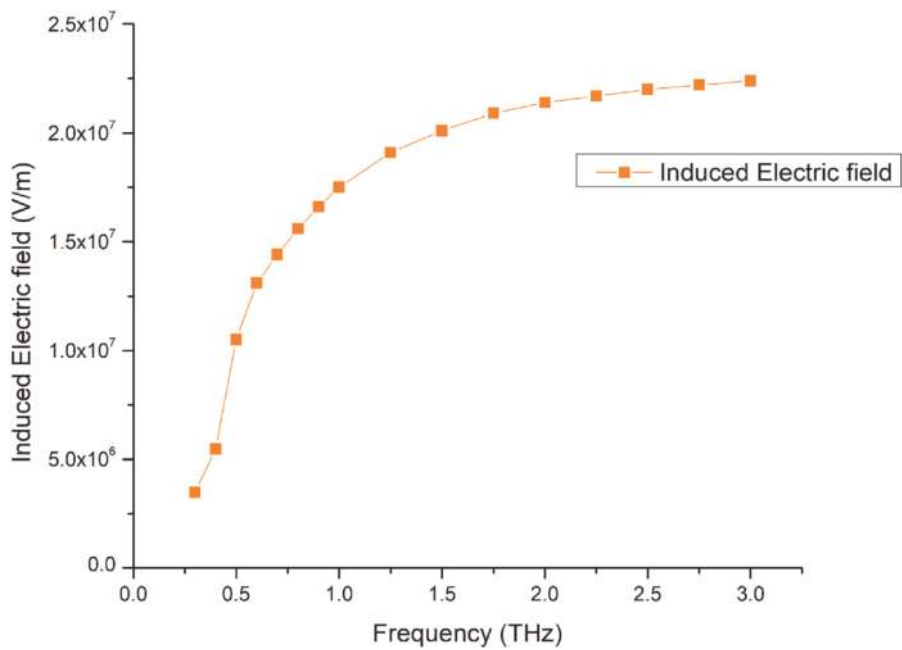

Figure 13.
Induced electrical field due to terahertz radiation illumination on GaN HEMT device using a finite element method-based electromagnetic solver (COMSOL).

greater than the externally applied bias field ($\sim 10^4$ V/cm = 10^6 V/m) at the gate (**Figure 7**).

The outcome of the entire simulation activities clearly demonstrates GaN HEMT device operation in the THz range beyond its cut-off frequency. It is also shown that

overall performance of GaN HEMT is governed by aggregate effects of ISBT, plasmonic structure and metamaterial behavior.

3. Fabrication and measurement of GaN HEMT devices

In this section we report fabrication and measurement details for experimental investigation of room-temperature, photon-induced electrical tuning of ISBT in GaN HEMT, which extends the device operating frequency well beyond its present cut-off frequency [56]. For sample fabrication, an AlGaN/AlN/GaN-based heterostructure was grown by metalorganic chemical vapor deposition (MOCVD) on 6H polytype of silicon carbide (6H-SiC) wafer. The layer sequence, thickness and composition were kept identical as used in our modeling and simulation work (**Figure 1(a)**). A 60-nm aluminum nitride (AlN) nucleation layer was grown on (0001) the face of a semi-insulating silicon carbide (SI–SiC) wafer. In the MOCVD growth, unintentionally doped (UID) GaN buffer layer thickness was set to ∼2 μm. On the top of the GaN buffer layer, a 1-nm AlN spacer layer followed by an undoped $Al_{0.3}Ga_{0.7}N$ barrier layer was grown to form a triangular quantum well of GaN HEMT. A small 3-nm Si_3N_4 passivation layer was kept as a top protective layer. For the purpose of characterization of this GaN heterostructure to assess quality and properties, highly precise standard semiconductor characterization tools like Hall measurement (nanomagnetic instruments), high-resolution XRD (Bruker D8 Discover), photoluminescence (PL) system (DongWoo Optron), and others were used. Room-temperature mobility and 2DEG carrier concentration were measured using the Hall measurement method. Composition, thickness and lattice constants for heterostructure materials were extracted using HR-XRD. The growth quality was evaluated using the PL method.

A standard fabrication process flow as shown in **Figure 14** was adopted for GaN HEMT device fabrication. Device-to-device isolation was performed by MESA
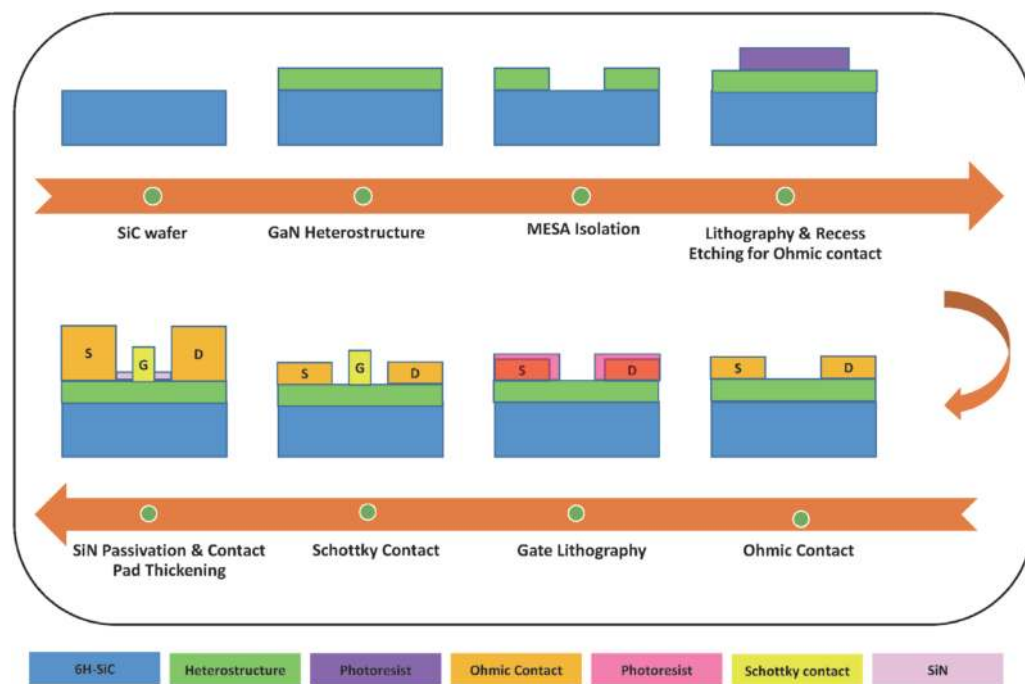

Figure 14.
GaN HEMT fabrication flow along with the cross-sectional view of the device.

etching using $BCl_3/Cl_2/Ar$ dry plasma. An inductively coupled plasma-reactive ion etching (ICP-RIE) system was used for HEMT device isolation. Source-drain spacing was kept at 3.0 micron and electron beam lithography was used for ohmic contact (source and drain) patterning. Recess etching of the barrier AlGaN layer was required to fabricate good ohmic contacts. An optimized recessed etching process was followed to etch ~10 nm of the AlGaN layer using $BCl_3/Cl_2/Ar$ plasma. During recess, $BCl_3/Cl_2/Ar$ flow rates were maintained at 20/10/10 SCCM with ICP power and RF power at 350 W and 60 W, respectively. Post recess, the sample was dipped in HCl:DI (1:10) for one minute to minimize the impact of oxidation on the surface. A Ti/Al/Ni/Au (20/210/55/45 nm) lift-off metallization scheme was selected and deposited by electron beam evaporation for ohmic contact. The sample was annealed at 870°C for 45 s under N2 atmosphere using rapid thermal annealing to form the ohmic contact [57]. The ohmic contact resistance was measured using a standard transmission line model (TLM) with the help of a semiconductor characterization system (Model Keithley 4200). Electron beam lithography was used to form a mushroom gate contact. A Ni/Au metallization scheme was selected for gate contact to achieve high Schottky barrier height. A Ni/Au (30/300 nm) stack was deposited using electron beam evaporation and lift-off technique followed by annealing at 450°C for 120 s under N2 atmosphere using rapid thermal annealing system [58]. To address the DC-RF dispersion issue, the Si_3N_4 passivation layer of 120-nm thickness was deposited using PECVD. Contact pad thickening was formed by 800-nm Ti/Au deposition to reduced resistive loss. The fabricated GaN HEMT wafer (1 square inch) having more than 300 GaN HEMT devices is shown in **Figure 15**. A sufficient number of variants are kept in fabrication in terms of device length and number of device fingers for wider statistical data. Device length varies from 50 to 300 micron (50, 100, 150, 200, 300), while number of fingers varies from 2 to 12 (2, 4, 6, 8, 10, 12). All devices have a 100-nm mushroom gate structure. The wafer also contains varieties of process control monitors (PCMs) for ohmic contact, Schottky contact, short, open and through the structure for RF measurement.

Current–voltage (IV) measurements on the fabricated sample were performed using a highly accurate and precise Keithley 4200 source measurement unit (SMU) inside a vacuum chamber equipped with a Janis probe station and Lakeshore temperature controller. IV measurements were performed in dark mode
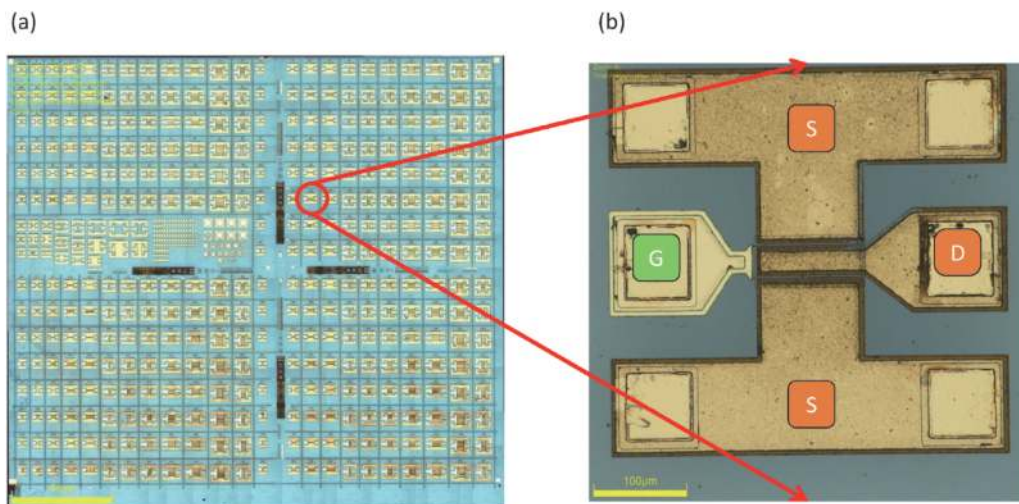

Figure 15.
(a) GaN HEMT fabricated wafer (b) 100°nm 2 × 100 GaN HEMT device (reprinted with permission from Ref. [56]).

(no illumination) and radiation illumination mode to extract the ISBT in fabricated GaN HEMT devices. 1-mW blue, yellow and red LEDs as well as 300-W halogen lamp-based perpendicular illumination sources were used in our experiment to excite the deep-level traps in the GaN HEMT device, while 1-mW broadband infrared illumination sources like a red laser (630–690 nm), near-infrared (NIR) LED (650–850 nm) and short-wave infrared (SWIR) LED (1.7–2.1 micron) based illumination at an oblique angle of incident (AOI) were used to investigate the ISBT at ambient temperature. Moreover, to confirm the transition is solely dependent upon the bandgap phenomenon, low-temperature PL and IV measurements were also carried out. Most devices showed the ambient temperature ISBT, however, we selected the 2×100 device for demonstration.

4. Results and discussion on experimental outcome

Post growth, the GaN heterostructure was extensively evaluated using standard, highly accurate semiconductor characterization techniques. **Table 3** shows the summary of extracted heterostructure properties using various characterization techniques. Room-temperature mobility and 2DEG carrier concentration were found to be 1885 cm^2/V.s and 1.1E + 13 cm^{-2}, respectively, using the Hall measurement method. The composition and thickness of the AlGaN barrier layer play crucial roles in polarization and 2DEG carrier accumulation inside the GaN HEMT. Thickness of 21 nm and Al composition of 31% were found in the AlGaN barrier layer against targeted thickness of 20 nm and Al composition of 30%. Ohmic and Schottky contacts to GaN heterostructures play a vital role in the development of a GaN HEMT device. Low contact resistance of ~0.27 Ω.mm and high barrier height of ~0.72 eV were extracted using IV measurements. Surface traps were present in the GaN HEMT devices and led to significant degradation of DC and RF performance. High-quality Si_3N_4 surface passivation deposition was used to effectively reduce surface traps. The improvement in drain current density is about 35 mA/mm and in RF gain is 4 dB at 10 GHz after Si_3N_4 deposition, which clearly indicates the majority of surface traps are saturated after passivation. The saturation drain current density (@ Vg = 0 V) was measured at ~1 A/mm, while cut-off frequency of ~89 GHz was extracted for the fabricated 100-nm GaN HEMT.

FET shows the response towards THz beyond its cutoff frequency even at room temperature irrespective of semiconductor material systems [22, 24–28]. The Dyakonov–Shur plasma wave theory [22, 23] classically explains the THz behavior of the device starting from conventional semiconductors like Si, GaAs, and GaN to recently developed 2D materials system like graphene, MoS_2, WS_2, black phosphorous, and others. We proposed ISBT transition at ambient temperature as another

Properties	AlGaN	GaN	Measurement method
Thickness	21 nm	2.0	HR-XRD
Composition (%)	$Al_{0.31}Ga_{0.69}N$	—	HR-XRD
Lattice constant (A°)	5.121	5.185	HR-XRD
Bang gap (eV)	—	3.44	PL
2DEG	—	1.1E+13	Hall
Mobility (RT)	—	1885	Hall

Table 3.
Measured heterostructure properties using standard semiconductor characterization equipment.

potential mechanism for THz response of the GaN HEMT device. ISBT is demonstrated using IV measurement of the GaN HEMT device under dark and illuminated conditions. Usually, IV characteristics are the combination of all possible phenomenon in the FET. It is very difficult to distinguish the defects- or traps-assisted transitions, thermal transitions and ISBTs in the IV characteristics of FET. However, electrical tuning of ISBT in GaAs HEMT has been demonstrated [59]. There are three following key challenges involved in supporting the ambient ISBT mechanism in FET/HEMT.

1. rule out plasma wave mechanism

2. Defects−/traps-based transitions

3. Thermal energy-assisted transitions

4.1 Rule out plasma wave mechanism

The basic physics involved in plasma wave theory is that 2DEG instability in short-channel HEMTs has a resonant response to incident electromagnetic radiation. The resonance frequency is governed by the size and shape of the channel (i.e., the geometrical plasmon frequency). Tuning the plasmon resonant frequency to the incident THz wave is used for detectors, mixers and multipliers, as the carrier resonance happens in the THz frequency range only. It is not possible to generate plasma wave inside the FET channel if the incident radiation has a frequency other than THz. In other words, if we are using a source other than a THz radiation source that is capable of inducing the ISBT, the generation of plasma waves can be ruled out inside the FET/HEMT.

4.2 Defects/traps-based transitions

The deep-level traps- or defects-assisted transitions have been well reported since the invention of heterostructure [60]. The traps' energy level and density depend upon several parameters like heterostructure growth condition, materials system, and others. Especially in GaN-based wide bandgap semiconductor materials, the domination of the deep-level traps is even more significant than GaAs semiconductor material [61]. It is highly difficult to prevent the transitions through these traps. However, control over traps-based transition is possible, as it shows the different responses towards the incident radiations. If we are selecting the illumination source that has the least significance for trap excitation and the most significance for ISBT, then defects−/traps-assisted transitions can also be also ruled out.

4.3 Thermal energy-assisted transitions

The thermal energy associated at room temperature is ∼25 mev (∼ 6 THz), which is much higher than the spacing between the subband in a quantum well. It is very difficult to negligible thermal energy contribution. Thermal occupation of electrons in a higher subband may prevent the observation of ISBT at ambient temperature [59]. Measurement are done at ambient as well as low temperature in vacuum condition with a precise and accurate temperature controller to quantified the thermal transitions. Furthermore, source-measurement units (SMUs) are accurate for detecting very small changes in measurement for dark and illuminated conditions. The background thermal energy contribution in transitions is equally

present in both dark and illumination modes, which clearly indicates the presence of ISBT in the measurement.

In summary, to confirm the transitions solely occurring due to ISB inside the triangular quantum well of the heterostructure, we used a 1-mW SWIR LED because it is least significant for trap excitation [62, 63], whereas it is most significant for ISBT. Moreover, the use of a SWIR source that is not in the THz frequency range ensures that the generation of plasma wave inside the channel is not possible. The blue LED was selected for measuring traps-assisted transitions. **Table 4** summarizes the key challenges involved along with possible solutions to confirm room-temperature ISBT in GaN HEMT.

To excite the deep-level traps in a GaN heterostructure, 1-mW blue, yellow and red LEDs as well as a 300-W halogen lamp-based perpendicular illumination were used. It is well proven that as we move from NIR to UV radiations, the trap excitation becomes more efficient. It is difficult to excite traps larger than 870 nm [62, 63]. In our experiments, blue LED was found to be more efficient among all used light sources to excite the deep-level traps. To extract the trap-assisted transitions, a 90-degree AOI under blue LED illumination for 10 min was used. The Id-Vd characteristics and change in drain current (ΔId) of the 100-nm GaN HEMT without and with illumination are shown in **Figure 16(a)**. Deep-level traps-assisted transitions increased the drain current up to approximately 24 mA/mm as shown in **Figure 16(b)**. It was found that after 10 min of illumination, there was no further significant increase in drain current, which confirms that most traps were saturated and the equilibrium condition was reached.

Sr. No	Discrimination ISBT from other mechanism	Used excitation source/methods
1	Plasma wave mechanism	Non terahertz radiation source
2	Defects/traps induced transition	Blue LED
3	Thermal energy contribution	Measurement in vacuum, precise temperature control with highly accurate SMUs Confirm with low temperature IV and PL
4	ISBT	SWIR (1.7–2.1 μm) source

Table 4.
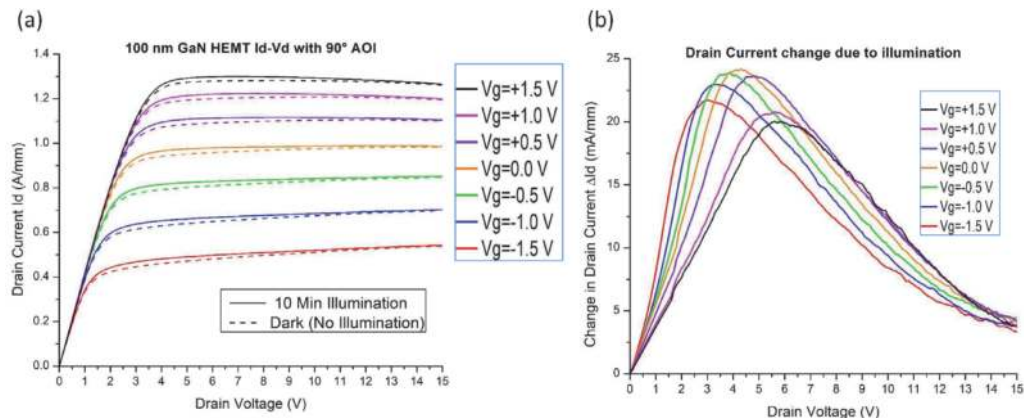*Measurement methods and excitation sources used to confirm ISBT.*

Figure 16.
Effect of 90° AO Iillumination with blue LED (a) on id-Vd characteristics of 100 nm GaN HEMT device (b) change in drain current (reprinted with permission from Ref. [56]).

Red laser (630–690 nm), NIR LED (650–850 nm) and SWIR LED (1.7–2.1 micron) broadband infrared sources were used in our experiment to investigate physical phenomena other than plasma wave at ambient temperature. It is noted that the ISB absorption characteristics were found to be identical for all used IR sources (red laser, NIR and SWIR LEDs) with the highest absorption found for the case of SWIR LED.

For ISBT experiments, we selected 1-mW SWIR LED as it is least significant for trap excitation [62, 63], whereas it is most significant for ISBT. GaN heterostructure materials have a wide bandgap with lower cut-off wavelengths than the wavelength of the IR light source, ensuring the transition of the carriers from valance band to the conduction band is forbidden.

When light is incident perpendicular to the sample surface ISBT cannot be induced, as the electric field has component only in the quantum-well plane [40]. We illuminated the sample at an oblique angle of incidence to discriminate ISBT with other transitions. When the sample is illuminated with an oblique angle, IR radiation interacts with carriers inside the subband of the triangular quantum well and transitions occur within the conduction band. The Id-Vd characteristics and change in drain current (ΔId) of the 100-nm GaN HEMT without and with 30 s of 45-degree AOI SWIR LED illumination are shown in **Figure 17(a)** and **(c)**. A zoom portion of the Id-Vd curve for -0.5 and -1.0 gate voltage is shown in **Figure 17(b)** for visualization purposes, as the change in drain current was very small due to illumination. Infrared lamp-assisted photoinduced ISBT in doped and undoped multiple quantum wells was reported by Olszakier et al. in a series of experiments [64–68]. It was concluded that the ISBT involves free electrons as well as excitons. The exciton-based transitions have greater frequency and oscillator strength than those of the bare electrons.

The bulk wurtzite semiconductor band diagram along with the two E_0 and E_1 subbands in the triangular quantum well involves transition of free electrons and excitons-based transition as shown in **Figure 18(a)**–**(c)**, respectively. In the asymmetrical (triangular) quantum well, inversion symmetry with respect to the quantum well center is broken, which leads to a relaxation of the selection rules (i.e., transitions between all subbands are allowed) [40]. It is possible to tune subbands inside the quantum well by external electrical field in an HEMT device. Free electron-based ISBT (0.5–10 THz) and exciton-assisted ISBT (for higher frequency) can be exploited as potential tunable sources and detectors for the entire THz range.

The spacing between subband and quantum-well width depends on gate biasing. Let us consider only two subbands, E_0 and E_1 inside a well having N_0 and N_1 electrons, respectively. The gate voltage is selected in such a way where ground state E_0 is situated below the Fermi level as shown in **Figure 19(a)**. The 2DEG
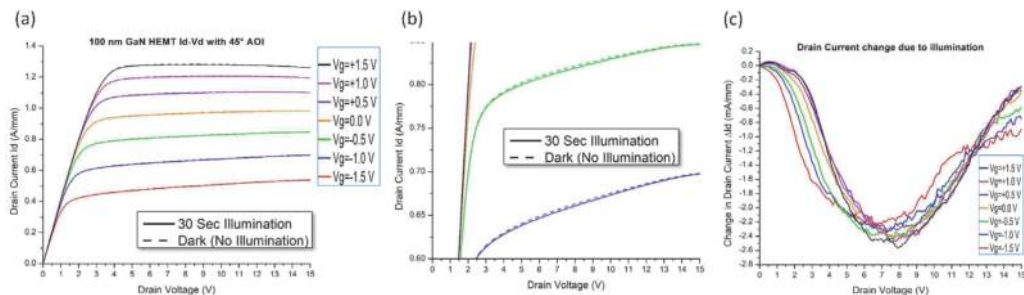

Figure 17.
Effect of 45° AO Iillumination with SWIR led (a) on id-Vd characteristics of 100°nm GaN HEMT device (b) zoom portion of id-Vd characteristics for drain current change visualization and (c) change in drain current (reprinted with permission from Ref. [56]).
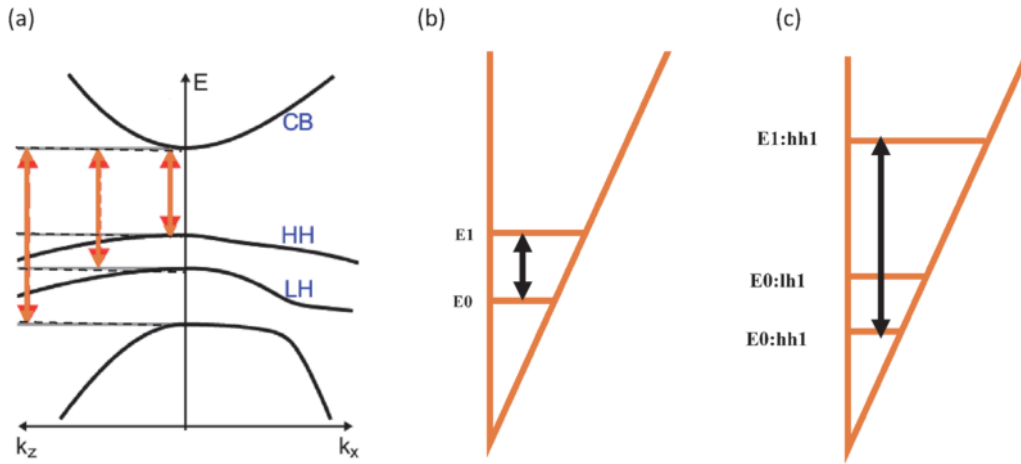
Figure 18.
(a) Band structure for wurtzite (WZ) bulk semiconductor with conduction band (CB), light and heavy holes (HH, LH). The ISBT is shown in (b) well electrons and (c) the exciton schemes. (reprinted with permission from Ref. [56]).
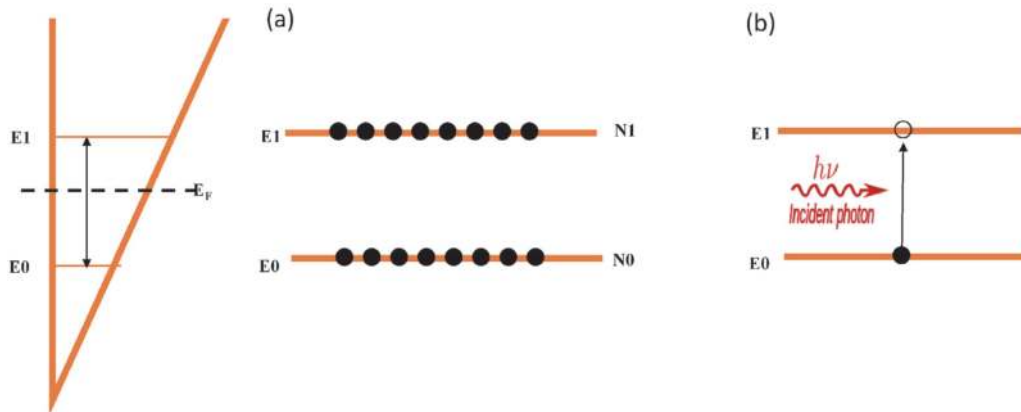

Figure 19.
(a) Band-schematic of the first two subbands in a 2DEG with respect to the Fermi level (b) absorption in the subband. (reprinted with permission from Ref. [56]).

carriers below the Fermi energy level are extracted as a drain current by applying a potential between source and drain. When the sample is illuminated, the electrons in a ground state E_0 interact with an external electromagnetic field. The electrons pick up photons from the illuminating field, which allows them to enter an excited energy state E_1 within the subband as shown in **Figure 19(b)**. These excited electrons are in the energy level E_1 that is above the Fermi level. As these electrons are not contributed to conduction, the drain current Id is decreased. This mechanism is clearly observed in **Figure 17(c)** in terms of decrease in drain current due to illumination, which shows ISB absorption. The amount of absorption strictly depends upon the distribution of electrons in the subband and the spacing between subband and width of well. To rule out thermal energy contribution in IV characteristics, measurement is done in vacuum conditions. The precise and accurate temperature controller and SMUs are used in measurement, which are able to detect a very small change in drain current in dark and illuminated conditions. Moreover, to confirm the transition is solely dependent upon the bandgap phenomenon, low-temperature PL and IV measurements were carried out. The temperature-dependent bandgap shifting in GaN found in PL measurement, as shown in

Figure 20, matches with previously published results [69]. Low-temperature 200-K and 100-K ISB absorption measurements were also carried out. It was found that the intensity of absorption increases as the temperature decreases, as shown in **Figure 21(a)** and **(b)**. It indicates that thermal energy contribution decreases with a decrease in temperature. The temperature-dependent bandgap variation in GaN perfectly matches with ISB absorption (Vg = 0 V, Vds = 8 V), as depicted in **Figure 22**.

In conclusion, low-temperature and angle-dependent illumination-based measurements were used to confirm the ISB transition in GaN HEMT. We have
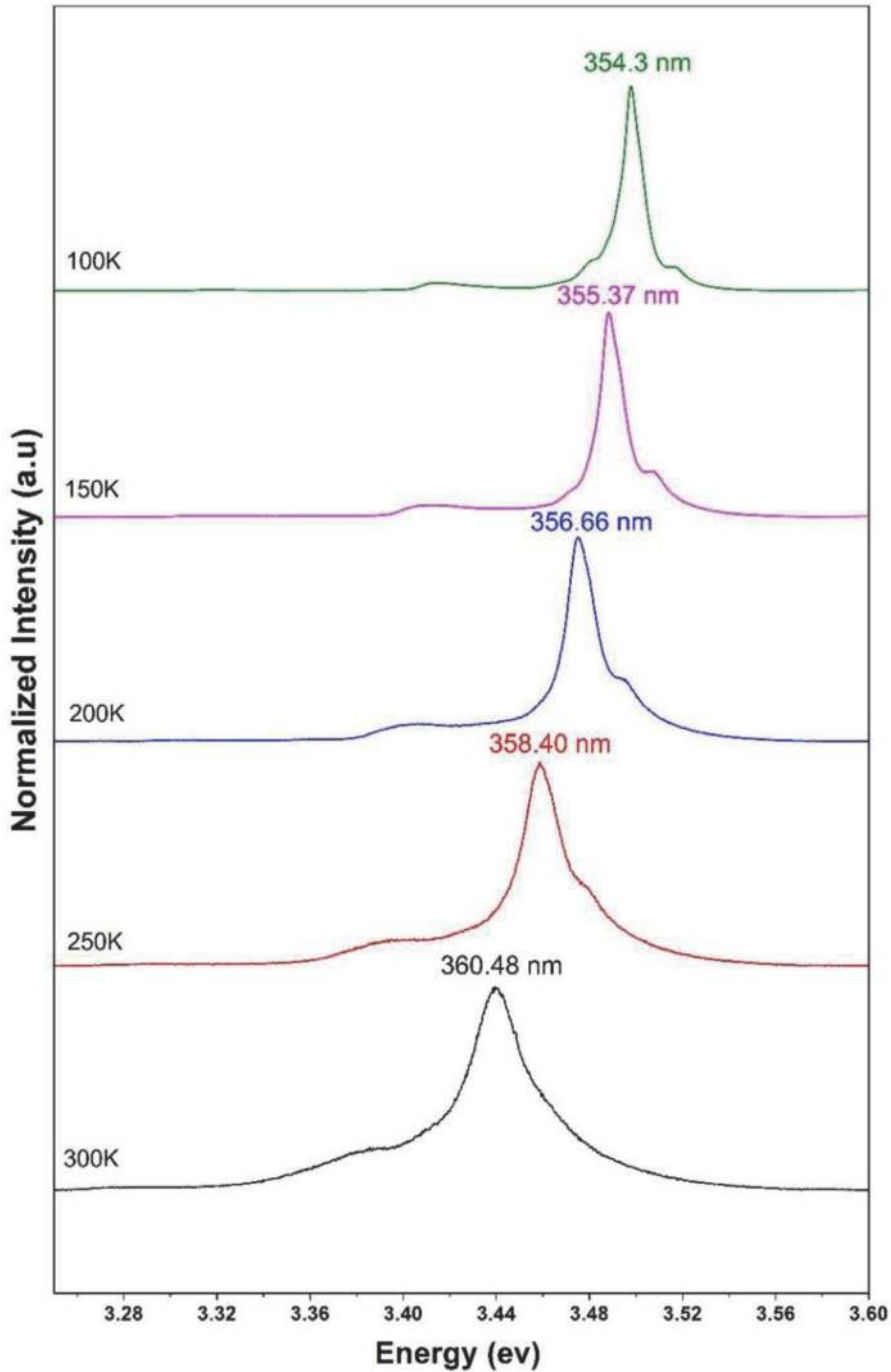

Figure 20.
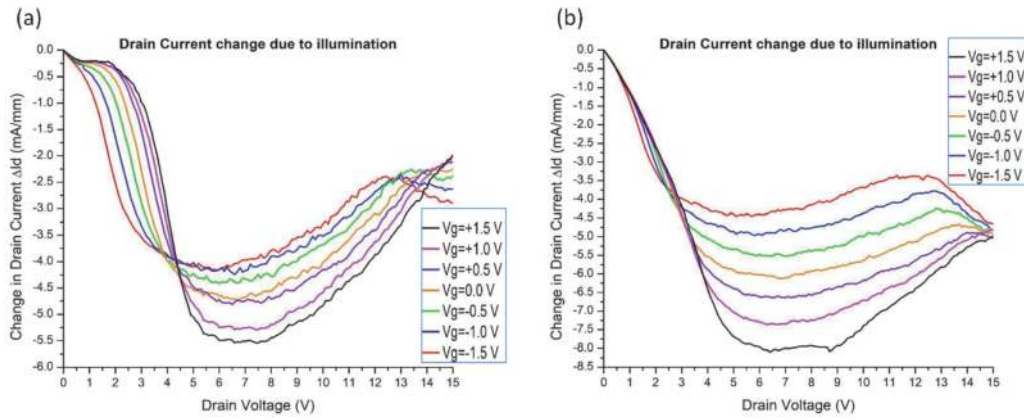*Low-temperature PL measurement of GaN heterostructure (reprinted with permission from Ref. [56]).*

Figure 21.
Change in drain current due to 45° AOI and 30°second illumination with SWIRLED at temperature (a) 200 K and (b) 100 K (reprinted with permission from Ref. [56]).
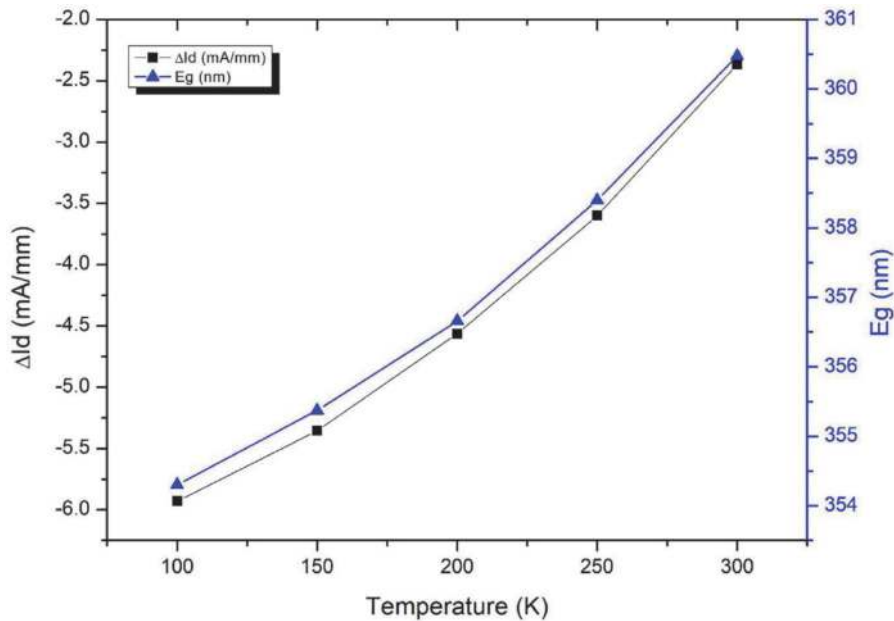

Figure 22.
Temperature dependent GaN band gap and change in drain current (vg = 0 V and Vds = 8 V) due to illumination (reprinted with permission from Ref. [56]).

experimentally explored electrical tuning of ISB resonance phenomena inside the triangular quantum well for a GaN HEMT device, which shows the potential of GaN HEMT technology to be realized as a room-temperature THz source and detector.

5. Conclusion

We have developed theoretical models for electrically tunable plasmonic metamaterials-assisted ISBT in GaN HEMT. Experimental demonstration of electrical tuning of ISBT in a GaN HEMT device at room temperature has not only provided a new alternate mechanism but also discriminates ISBT from other transitions induced by deep-level traps and defects in the 100-nm GaN HEMT device. The chapter also explored the photonics ISBT phenomenon in a GaN HEMT device

for external biasing, which depends on tuning of the subband. A novel approach for ISBT in GaN HEMT helps to overcome the THz gap in the electromagnetic spectrum at ambient temperature.

Acknowledgements

Author details

Rakesh Kaneriya[1,2*], Gunjan Rastogi[1], Palash Basu[3], Rajesh Upadhyay[1] and Apurba Bhattacharya[1]

1 Microelectronics Group, Space Applications Centre, ISRO, Ahmedabad, India

2 Department of Physics, Indian Institute of Space Science and Technology, Thiruvananthapuram, India

3 Department of Avionics, Indian Institute of Space Science and Technology, Thiruvananthapuram, India

*Address all correspondence to: rakeshk@sac.isro.gov.in

IntechOpen

References

[1] Tonouchi M. Cutting-edge THz technology. Nature Photonics. 2007;**1**: 97-105. DOI: 10.1038/nphoton.2007.3

[2] Xiang Yang, Xiang Zhao, Ke Yang, Yueping Liu, Yu Liu, Weiling Fu, Yang Luo. Biomedical applications of terahertz spectroscopy and imaging. Trends in Biotechnology. **34**(10);2016: 810-824

[3] Mittleman DM. Twenty years of terahertz imaging. Optics Express. 2018; **26**:9417-9431

[4] Rahman A, Rahman AK, Rao B. Early detection of skin cancer via terahertz spectral profiling and 3D imaging. Biosensors & Bioelectronics. 2016;**82**: 64-70

[5] Nagai N, Sumitomo M, Imaizum M, Fukasawa R. Characterization of electron- or proton irradiated Si space solar cells by THz spectroscopy. Semiconductor Science and Technology. 2006;**21**:201-209

[6] Nagai N, Imai T, Fukasawa R, Kato K, Yamauchi K. Analysis of the intermolecular interaction of nanocomposites by THz spectroscopy. Applied Physics Letters. 2004;**85**: 4010-4012

[7] Siegel P. THz instruments for space. IEEE Transactions on Antennas and Propagation. 2007;**55**(11):2957-2965

[8] Siegel PH. THz for space: The golden age. 2010 IEEE MTT-S International Microwave Symposium, 2010. pp. 816-819. DOI: 10.1109/ MWSYM.2010.5515761

[9] Ferguson B, Zhang XC. Materials for terahertz science and technology. Nature Materials. 2002;**1**:26-33. DOI: 10.1038/nmat708

[10] Khanal S, Zhao L, Reno JL, Kumar S. Temperature performance of terahertz quantum-cascade lasers with resonant-phonon active-regions. Journal of Optics. 2014;**16**:094001. DOI: 10.1088/ 2040-8978/16/9/094001

[11] Rastogi G, Kaneriya RK, Sinha S, Upadhyay RB, Bhattacharya AN. Physics based simulation for studying the impact of contact resistance on DC and RF characteristics of AlGaN/AlN/ GaN HEMT. Journal of Radio Science. 2019;**54**:904

[12] Kaneriya RK, Rastogi G, Basu PK, Upadhyay RB, Bhattacharya AN. Intersubband device modeling of gallium nitride high electron mobility transistor for terahertz applications. Journal of Radio Science. 2019;**54**:1172-1180. DOI: 10.1029/ 2019RS006844

[13] Kaneriya RK, Rastogi G, Basu PK, Upadhyay RB, Bhattacharya AN. Modeling of Electrically Tunable Metamaterial Embedded Intersubband Transitions in GaN HEMT for Terahertz Applications. 2020 URSI Regional Conference on Radio Science (URSI-RCRS), 2020, pp. 1-5, doi: 10.23919/ URSIRCRS49211.2020.9113510

[14] Smorchkova IP, Chen L, Mates T, Shen L, Heikman S, et al. AlN/GaN and (Al,Ga)N/AlN/GaN two-dimensional electron gas structures grown by plasma-assisted molecular-beam epitaxy. AIP Publishing LLC. Journal of Applied Physics. 2001;**90**:5196. DOI: 10.1063/ 1.1412273

[15] Shen L, Heikman S, Moran B, Coffie R, Zhang N-Q, Buttari D, et al. AlGaN/AlN/GaN high-power microwave HEMT. IEEE Electron Device Letters. 2001;**22**:10

[16] Bernardini F, Fiorentini V, Vanderbilt D. Spontaneous polarization and piezoelectric constants of III-V nitride. Physical Review B. 1997;**56**:10024

[17] Weiwei K. TCAD simulation and modeling of AlGaN/GaN HFET [thesis]. 2008, North Carolina State University, Raleigh, North Carolina

[18] Silvaco® Application Note. State of the art 2D and 3D process and device simulation of GaN-based devices. A Journal for Process and Device Engineers. 2013;**23**(3):1-11

[19] Silvaco® Application Note. Atlas Simulation of GaN-Based Super Heterojunction Field Effect Transistors Using the Polarization Junction Concept, Simulation Standard. 2014

[20] Albrecht JD, Wang RP, Ruden PP, Farahmand M, Brennan KF. Electron transport characteristics of GaN for high temperature device modeling. Journal of Applied Physics. 1998;**83**(9):4777-4781. DOI: 10.1063/1.367269

[21] Yue Y, Hu Z, Guo J, Rodriguez BS, Li G, Wang R, et al. InAlN/AlN/GaN HEMTs with regrown ohmic contacts and fT of 370 GHz. IEEE Electron Device Letters. 2012;**33**(7):988-990. DOI: 10.1109/LED.2012.2196751

[22] Dyakonov M, Shur M. Shallow water analogy for a ballistic field effect transistor: New mechanism of plasma wave generation by dc current. Physical Review Letters. 1993;**71**(15): 2465-2468. DOI: 10.1103/PhysRevLett.71.2465

[23] Dyakonov M, Shur M. Detection, mixing, and fequency multiplication of terahertz radiation by two-dimensional electronic fluid. IEEE Transactions on Electron Devices. 1996;**43**(3):380-387. DOI: 10.1109/16.485650

[24] Nahar S, Shafee M, Blin S, Penarier A, Nouvel P, Coquillat D, et al. Wide modulation bandwidth terahertz detection in 130 nm CMOS technology Eur. Journal of Applied Physics. 2016; **76**:20101. DOI: 10.1051/epjap/2016160302

[25] Hou HW, Liu Z, Teng JH, Palacios T, Chua SJ. High temperature terahertz detectors realized by a Gan high electron mobility transistor. Scientific Reports. 2017;**7**:46664. DOI: 10.1038/srep46664

[26] Kurita Y, Ducournau G, Coquillat D, Satou A, Kobayashi K, Tombet SB, et al. Ultrahigh sensitive sub-terahertz detection by InP-based asymmetric dual-grating-gate high-electron-mobility transistors and their broadband characteristics. Applied Physics Letters. 2014;**104**:251114. DOI: 10.1063/1.4885499

[27] Wang L, Chen X, Yu A, Zhang Y, Ding J, Lu W. Highly sensitive and wide-band tunable terahertz response of plasma waves based on graphene field effect transistors. Scientific Reports. 2014;**4**:5470. DOI: 10.1038/srep05470

[28] Viti L, Hu J, Coquillat D, Politano A, Knap W, Vitiello MS. Efficient terahertz detection in black-phosphorus nano-transistors with selective and controllable plasma-wave, bolometric and thermoelectric response. Scientific Reports. 2016;**6**:20474. DOI: 10.1038/srep20474

[29] Sun JD, Sun YF, Wu DM, Cai Y, Qin H, Zhang BS. High-responsivity, low-noise, room-temperature, self-mixing terahertz detector realized using floating antennas on a GaN-based field-effect transistor. Applied Physics Letters. 2012;**100**:013506. DOI: 10.1063/1.3673617

[30] Javadi E, Delgado-Notario JA, NMasoumi MS, Elazquez-Perez VJE, Meziani YM. Continuous wave terahertz sensing using GaN HEMTs. Physica Status Solidi (a) 215 (2018): 1700607

[31] Hou HW, Liu Z, Teng JH, Palacios T, Chua SJ. A sub-terahertz broadband detector based on a GaN high-electron-mobility transistor with nanoantennas.

Applied Physics Express. 2017;**10**: 014101. DOI: 10.7567/APEX.10.014101

[32] Fatimy A, Dyakonova N, Meziani Y, Otsuji T, Knap W, Vandenbrouk S, et al. AlGaN/GaN high electron mobility transistors as a voltage-tunable room temperature terahertz sources. Journal of Applied Physics. 2010;**107**:024504. DOI: 10.1063/1.3291101

[33] Chuang SL. Physics of Optoelectronic Devices. New York: John Wiley and Sons; 1995

[34] Chuang SL. Physics of Photonics Devices. New York: John Wiley and Sons; 2009

[35] Bradley AF. Envelope-function formalism for electrons in abrupt heterostructures with material-dependent basis functions. Physical Review B. 1996;**54**:1909-1921

[36] Eissfeller T, Vogl P. Real-space multiband envelope-function approach without spurious solutions. Physical Review B. 2011;**84**(19):195122. DOI: 10.1103/PhysRevB.84.195122

[37] Foreman BA. Effective mass Hamiltonian and boundary conditions for the valence bands of semiconductor microstructures. Physical Review B. 1993;**48**(7):4964-4967. DOI: 10.1103/ PhysRevB.48.4964

[38] Wieck AD, Thiele F, Merkt U, Ploog K, Weimann G, Schlapp W. Subband-landau-level coupling in GaAs/ Ga1−xAlx As heterojunctions. Physical Review B. 1989;**39**(6):3785-3794. DOI: 10.1103/PhysRevB.39.3785

[39] Ando T, Fowler AB, Stern F. Electronics properties of two dimensional systems. Reviews of Modern Physics. 1982;**54**(2):437–672. DOI: 10.1103/RevModPhys.54.437

[40] Helm M. The basic physics of intersubband transitions. In: Liu H, Capasso F, editors. Intersubband Transitions in Quantum Wells: Physics and Device Applications I, Semiconductors and Semimetals. Vol. 62. Academic Press; San Diego, CA, USA; 1999. pp. 20, 26

[41] Scalari G, Maissen C, Hagenmüller D, De Liberato S, Ciuti C, Reichl C, et al. Ultrastrong light-matter coupling at terahertz frequencies with split ring resonators and inter-Landau level transitions. Journal of Applied Physics. 2013;**113**:136510

[42] Benz A, Montaño I, Klem JF, Brener I. Tunable metamaterials based on voltage controlled strong coupling. Applied Physics Letters. 2013;**103**: 263116

[43] Scalari G, Maissen C, Turcinková D, Hagenmüller D, De Liberato S, Ciuti C, et al. Ultrastrong coupling of the cyclotron transition of a 2D electron gas to a THz metamaterial. Science. 2012; **335**:1323

[44] Gabbay A, Brener I. Theory and modeling of electrically tunable metamaterial devices using intersubband transitions in semiconductor quantum wells. 2012 Optical Express 20(6):6548

[45] Benz A, Campione S, Liu S, Montano I, Klem JF, Sinclair MB, et al. Monolithic metallic nanocavities for strong lightmatter interaction to quantum-well intersubband excitations. Optical Express. 2013; **21**(26):32572

[46] Shrekenhamer D, Rout S, Strikwerda A, Bingham C, Averitt RD, Sonkusale S, et al. High speed terahertz modulation from metamaterials with embedded high electron mobility transistors. Optical Express. 2011; **19**(10):9968

[47] Zhang Y, Zhao Y, Liang S, Zhang B, Wang L, Zhou T, et al. Large phase

modulation of THz wave via an enhanced resonant active HEMT metasurface. Nano. 2018;**8**(1):153

[48] Vicarelli L, Vitiello MS, Coquillat D, Lombardo A, Ferrari AC, Knap W, et al. Graphene field-effect transistors as room-temperature THz detectors. Nature Materials. 2012;**11**:865

[49] Zak A, Andersson M, Bauer M, Matukas J, Lisauskas A, Roskos H, et al. Antenna-integrated 0.6 THz FET direct detectors based on CVD graphene. Nano Letters. 2014;**14**(10):5834

[50] Tong J, Muthee M, Chen S, Yngvesson S, Yan J. Antenna enhanced graphene THz emitter and detector. Nano Letters. 2015;**15**(8):5295

[51] Viti L, Hu J, Coquillat D, Politano A, Knap W, Vitiello MS. Efficient terahertz detection in black-phosphorus nano-transistors with selective and controllable plasma-wave, bolometric and thermoelectric response. Scientific Reports. 2016;**6**:20474

[52] Berry C, Wang N, Hashemi M, Unlu M, Jarrahi M. Significant performance enhancement in photoconductive terahertz optoelectronics by incorporating plasmonic contact electrodes. Nature Communications. 2016;**4**:1622

[53] Tanoto H, Teng J, Wu Q, Sun M, Chen Z, Maier S, et al. Greatly enhanced continuous-wave terahertz emission by nano-electrodes in a photoconductive photomixer. Nature Photonics. 2012;**6**:121

[54] Wang N, Cakmakyapan S, Lin Y, Javadi H, Jarrahi M. Room-temperature heterodyne terahertz detection with quantum-level sensitivity. Nature Astronomy. 2019;**3**:977

[55] Yu N, Wang Q, Kats M, Fan J, Khanna S, Li L, et al. Designer spoof surface plasmon structures collimate terahertz laser beams. Nature Materials. 2010;**9**:730

[56] Kaneriya RK, Rastogi G, Basu PK, Upadhyay RB, Bhattacharya AN. Room temperature photon induced electrical tuning of intersubband transition in GaN HEMT for terahertz applications. Microelectronic Engineering. 2020;**233**: 111433

[57] Rastogi G, Kaneriya R, Sinha S, Upadhyay R. Optimization of ohmic contact fabrication for Al0.3Ga0.7N/ AlN/GaN HEMTs on 6H-SiC using recess etching and surface plasma treatment processes. Journal of Nanomaterials & Molecular Nanotechnology. 2019;**8**:2. DOI: 10.4172/2324-8777.1000267

[58] Rastogi G, Kaneriya R, Upadhyay R, Bhattacharya AN. Optimization of Ni/ Au Schottky contacts on Al0.3Ga0.7N/ AlN/GaN heterostructure for RF application. International Journal of Nanotechnology and Nanoscience. 2020;**6**:8-15

[59] Pal S, Valentin S, Ludwig A, Wieck A. Quantum Confinement in High Electron Mobility Transistors. IntechOpen, London, UK; 2017. DOI: 10.5772/intechopen.68374

[60] Mooney PM. Deep donor levels (DX centers) in III-V semiconductors. Journal of Applied Physics. 1990;**67**(3): R1. DOI: 10.1063/1.345628

[61] Polyakov AY, Lee IH. Deep traps in GaN-based structures as affecting the performance of GaN devices. Materials Science and Engineering. 2015;**94**:1-56. DOI: 10.1016/j.mser.2015.05.001

[62] Liang Y, Jia L, He Z, Fan Z, Zhang Y, Yang F. The study of the contribution of the surface and bulk traps to the dynamic Rdson in AlGaN/ GaN HEMT by light illumination.

Applied Physics Letters. 2016;**109**: 182103. DOI: 10.1063/1.4966536

[63] Polyakov A, Smirnov N, Shchemerov I, Lee H, Jang T, Dorofeev A, et al. Current relaxation analysis in AlGaN/GaN high electron mobility transistors. Journal of. Vacuum Science and Technology B. 2017;**35**:011207-1 to 10. DOI: 10.1116/1.4973973

[64] Olszakier M, Ehrenfreund E, Cohen E, Bajaj J, Sullivan GJ, Miller D. Intersubband spectroscopy in GaAs/GaAlAs multi-quantum-well structures: Photoinduced absorption. Superlattices and Microstructures. 1989;**5**:283. DOI: 10.1016/0749-6036(89)90301-7

[65] Olszakier M, Ehrenfreund E, Cohen E, Bajaj J, Sullivan GJ. Photoinduced intersubband absorption in undoped multi-quantum-well structures. Physical Review Letters. 1989;**62**:2997. DOI: 10.1103/PhysRevLett.62.2997

[66] Olszakier M, Ehrenfreund E, Cohen E, Bajaj J, Sullivan GJ. Intersubband absorption by photoinduced excitons in undoped multi quantum wells. Surface Science. 1989;**228**:123-126. DOI: 10.1016/0039-6028(90)90272-A

[67] Garini Y, Olszakier M, Cohen E, Ehrenfreund E, Ron A, Law KK, et al. Photoinduced intersubband absorption in barrier doped multi-quantum-wells. Superlattices and Microstructures. 1990;**7**:287-290. DOI: 10.1016/0749-6036(90)90211-O

[68] Cohen E, Ehrenfreund E, Garini Y, Olszakier M, Ron A. Photo-induced intersubband transitions in quantum wells. In: Rosencher E et al., editors. Lntersubband Transitions in Quantum Wells. New York: Plenum Press; 1992. p. 264

[69] Romero MF, Feneberg M, Moser P, Berger C, Bläsing J, Dadgar A, et al. Luminescence from two-dimensional electron gases in InAlN/GaN heterostructures with different In content. Applied Physics Letters. 2012; **100**:212101. DOI: 10.1063/1.4720087